Defect production and annealing kinetics in elemental metals and semiconductors [1]

T. Diaz de la Rubia [a,*], N. Soneda [b], M.J. Caturla [a], E.A. Alonso [a]

[a] *Lawrence Livermore National Laboratory, L-268, PO Box 808, Livermore, CA 94550, USA*
[b] *Central Research Institute of Electric Power Industry, 2-11-1 Iwado-kita, Komae-shi, Tokyo 201, Japan*

Abstract

We present a review of recent results of molecular dynamics (MD) and kinetic Monte Carlo (KMC) simulations of defect production and annealing in irradiated metals and semiconductors. The MD simulations describe the primary damage state in elemental metals Fe, V and Au, and in an elemental semiconductor Si. We describe the production of interstitial and vacancy clusters in the cascades and highlight the differences among the various materials. In particular, we discuss how covalent bonding in Si affects defect production and amorphization resulting in a very different primary damage state from the metals. We also use MD simulations to extract prefactors and activation energies for migration of point defects, as well as to investigate the energetics, geometry and diffusivity of small vacancy and interstitial clusters. We show that, in the metals, small interstitial clusters are highly mobile and glide in one dimension along the direction of the Burger's vector. In silicon, we show that, in contrast to the metals, the neutral vacancy diffuses faster than the neutral self-interstitial. The results for the primary damage state and for the defect energetics and kinetics are then combined and used in a kinetic Monte Carlo simulation to investigate the escape efficiency of defects from their nascent cascade in metals, and the effect of dose rate on damage accumulation and amorphization in silicon. We show that in fcc metals Au and Pb at or above stage V the escape probability is approximately 40% for 30 keV recoils so that the freely migrating defect fraction is approximately 10% of the dpa standard. In silicon, we show that damage accumulation at room temperature during light ion implantation can be significantly reduced by decreasing the dose rate. The results are compared to scanning tunneling microscopy experiments. © 1997 Published by Elsevier Science B.V.

1. Introduction

Irradiation effects in solids are a complex function of the interaction between the defects produced in displacement cascades and the material microstructure. At the shortest length (10–100 nm) and time scales (10–100 ps), energetic displacement cascades are responsible for the primary damage state. Because of the appropriateness of the length and time scale, displacement cascades can and have been studied extensively using MD simulations over the last 10 years [1,2]. At sufficiently elevated temperature, however, some or all of the produced defects are mobile and either recombine within or escape away from their nascent cascade. The fraction that escapes, the so-called freely migrating defect fraction, can then interact with the microstructure and cause compositional and mechanical property changes. These processes occur over much longer length and time scales than the cascade process and must therefore be investigated with methods other than MD.

In metals at low temperature, defect production in cascades is only approximately 30% as efficient [3] as the prediction of the linear theory [4]. These experimental results have been confirmed by MD simulation for many different metals [1,2,5]. At elevated temperatures, the fraction of freely migrating defects is more difficult to obtain, both experimentally and from simulations. Over the last 20 years, much experimental efforts have been devoted to

trying to extract this quantity. However, no consensus has been developed. For example, the FMD production efficiency, η, was studied experimentally in the Ni–Si system by monitoring radiation-induced segregation of the Si solute to the surface [6] and in pure Ni from measurement of radiation-enhanced diffusion [7]. However, analysis of the data from these experiments required many simplifying assumptions regarding possible defect reactions that could occur and the magnitude of the evolving sink strength in the material during irradiation. Moreover, the experiments measure a macroscopic change in a material property that results not only from the escape of defects from their nascent cascade, but is also governed by their interaction with the sink microstructure (dislocation, grain boundaries, etc.) and the debris from other cascades. It is very difficult to deconvolute all these factors from the experimental observations to obtain a number for the FMD production efficiency. Nevertheless, the experiments cited above obtained $\eta \approx 0.01$ (i.e. 1%) for the Ni–Si and the pure Ni cases. More recently, Fielitz et al. [8,9] have carried out a new set of experiments in Ni in which single crystal Ni samples were grown with embedded layers of isotonically pure ^{63}Ni and irradiated with Kr ions. The tracer was used as a diffusion marker during elevated temperature irradiation and a value of $\eta = 0.1$ (i.e. 10%) was obtained. Interpretation of the data required assumptions on the value of the sink strength of the material in this case as well, and the influence of the surface. Additional estimates of the production efficiency of FMDs have been obtained from void swelling experiments. For example, in Ni, swelling rates up to 5%/dpa (dpa = displacement per atom) have been observed [10] indicating that as many as 5% of the vacancies produced end up in voids. Since the fraction of freely migrating interstitials is not expected to be zero, the total fraction of FMDs is expected to be $\approx 10\%$ or larger from these experiments [8,9]. Diffuse X-ray scattering experiments following fission neutron irradiation of Cu and Ni after annealing below stage III have resulted in values of $\eta = 0.15$–0.25. Moreover, these experiments showed that most of the interstitials were in large loops with $r > 0.1$ nm [11].

Ion implantation is used routinely to dope silicon during semiconductor device manufacturing [12,13]. The implantation process uses ions such as B, As, P or Sb, at energies ranging from a few keV to 100 keV. The displacement cascades induced by these ions result in damage in the form of Frenkel pairs and amorphous zones. For device processing, the implanted silicon wafer must be annealed at elevated temperature in order to (1) remove the damage, and (2) activate the dopants. However, during annealing the dopant atoms interact with the implantation-induced defects and can diffuse over long distances [14]. As the size of devices becomes smaller, this phenomenon, known as transient enhanced diffusion (TED) becomes ever more critical [15]. As is the case for metals, the evolution of the defect microstructure during annealing

and the absolute magnitude of the TED effect depend critically on the form of the primary damage state and on the fraction of freely migrating defects.

In Section 2 we describe the simulation method, including both MD and kinetic Monte Carlo (KMC). In Section 3 we present the results obtained for both metals and semiconductor materials. Section 3.1 describes MD simulation results for the primary damage state in Au, Fe, V and Si. In Section 3.2 we present the application of the KMC simulation method to calculate defect annealing and migration in Fe at 600 K and in Si at various temperatures. We conclude with a summary in Section 4.

2. Simulation methodology

2.1. Molecular dynamics simulations

Simulations of defect energetics and kinetics, low energy recoil events, and high energy displacement cascades were all carried out with the MD simulation code, MD-CASK [16]. The vectorized link cell method [17] is originally used in MDCASK to fully vectorize the calculations of forces on vector-type supercomputers. This method is, however, still very suitable to modern engineering workstations with RISC processors because all the information required for the calculations in each link cell fits within the cash memory, meaning that the processor can execute operations at its maximum speed without any wait cycle for low-speed memory access. The performance on a DEC workstation with the 300 MHz Alpha chip is 1.2×10^{-4} CPU s/atom-MD step, equivalent to the performance on a vintage 1988 Cray 2 supercomputer. The classical equations of motion are integrated numerically using a fourth order predictor–corrector scheme. The time step, Δt, is automatically adjusted so that criteria for a maximum allowed displacement and a maximum allowed fractional energy change are satisfied for any atom in the crystal at any given step. Calculations can be carried out with periodic boundary conditions at either constant volume or constant pressure using the Parrinello–Rahman [18] scheme, but most of the calculations in the present study were performed at constant volume.

The Langevin equation of motion [19] is applied to the atoms in the link cells adjacent to the cell boundaries in order to control the temperature of the crystal. The resulting equation of motion is

$$m\ddot{x}_i = F_i + \eta_i(t) - \beta \dot{x}_i, \tag{1}$$

where m is the mass, $\ddot{x}_i$ are the coordinates of atom i, F_i is the force on atom i, β is the damping coefficient, and η_i is a random force that satisfies

$$\langle \eta_i(t) \rangle = 0, \qquad \langle \eta_i(t)\eta_i(t') \rangle = 2\beta kT\delta(t - t'), \tag{2}$$

with the distribution

$$P(\eta_i) = \left(2\pi\langle\eta_i^2\rangle\right)^{-1/2} \exp\left(\frac{-\eta_i^2}{2\langle\eta_i^2\rangle}\right).\qquad(3)$$

The boundary damping coefficient β was chosen to be 0.1 ps.

2.2. Interatomic potentials

2.2.1. BCC Fe

The analytic EAM interatomic potential for α-Fe developed by Johnson and Oh [20] and modified by Guellil and Adams [21,22] was used in our studies [23]. However, in order to apply this class of potentials to displacement cascade simulations, the repulsive pair interaction needs to be modified at short range to properly describe high energy scattering [24]. We first modified the pair-potential term by connecting it smoothly to the universal potential by Biersack and Ziegler [25], which gives a good representation of the interaction between two atoms at close separation. Interpolation between these two pair potentials is done using an exponential function of a third order polynomial. This exponential function guarantees the continuity of the first derivative as well as that of the function values. The atom distance range where these two functions are connected will be important in calculations of the displacement threshold energy. Since the Born–Mayer type is known to give a good approximation of the displacement threshold energy of α-Fe [26], following Calder and Bacon [27] we determined the interpolation range so that the interpolation function becomes close to the Born–Mayer potential. The resulting interpolation range is from 0.8 to 1.8 Å.

To make the interatomic forces identical to the ones calculated by the Ziegler–Biersack–Littmark universal potential [25] in the short distance range, the derivative of the embedding function term in this range should be negligible. To this end, we modified the electron density function by truncating it at $r = 1.8$ Å. The function was then smoothly connected to this truncation value using an exponential function of a polynomial in order to ensure the continuity of the first derivative, as in the case of the pair potential.

Interstitial and vacancy formation energies obtained using our modified Johnson and Oh's interatomic potential function are 4.33 eV and 1.73 eV, respectively, which agree well with the experimental values of 4.7 eV [28] and 1.6 eV [29,30], respectively. Interstitial atoms form dumbbells oriented along the $\langle110\rangle$ direction, in good agreement with experimental data for bcc metals [31]. The separation between the two atoms of the $\langle110\rangle$ dumbbell is $0.727a_0$, ($a_0 = 2.87$ Å is the lattice parameter), which agrees very well with the value of $0.725a_0$ obtained by Calder and Bacon [27] using the Finnis–Sinclair potential for α-Fe.

2.2.2. Au

For Au [32] we employed the standard EAM potential of Foiles et al. [33] after modification of the short range repulsive interaction following the same methodology described above [34]. With this potential, the calculated formation energies of the vacancy and the interstitial are 1.03 eV and 2.46 eV, respectively, in good agreement with experimental values [35]. We also investigated the activation energy for migration of both the vacancy and the interstitial. For the vacancy, we obtained a value of 0.97 eV, which means that the self-diffusion activation energy obtained is $Q = 2$ eV, again in good agreement with experiments [35]. For the self-interstitial atom (SIA), we obtained a migration energy of 0.08 eV, clearly higher than the expected from experiments where the interstitial in Au has been found to be mobile well below 4 K [36]. Nevertheless, the low activation energy obtained indicates that the potential is rather realistic, except that of course it does not describe possible tunneling effects that may give rise to the very low value of the activation energy observed experimentally.

2.2.3. Vanadium

For vanadium [37], we employed the Johnson and Oh interatomic potential [20]. We evaluated various other existing potentials by comparing the formation and migration energies of the vacancy and the fcc–bcc energy difference and compared the results to experiments and ab initio LMTO calculations [38]. The results for the Johnson–Oh potential show that $E_f = 2.02$ eV and $E_m = 0.7$ eV for the vacancy, which results in a self-diffusion activation energy of 2.73 eV which compares well to the experimental value of 2.9 eV. The fcc–bcc energy difference obtained with this potential was 0.2 eV, in reasonable agreement with the LMTO results (0.3 eV) [38]. We note that this was overall the best of all potentials evaluated for vanadium. We also carried out MD simulations to calculate the melting point and found a value of 2180 K, consistent with experiment. The most stable configuration of the SIA was found to be the $\langle110\rangle$ split dumbbell. This configuration was always obtained during dynamical simulations of the threshold energy for displacements or high energy cascades.

2.2.4. Silicon

Silicon is a covalently bonded semiconductor and therefore the standard EAM-type potentials cannot be used to carry out simulations. In our studies we have used the Stillinger–Weber potential [39] for silicon. This is a widely used and tested potential that reproduces the melting point of silicon and many other properties correctly. Although other potentials for silicon exist in the literature [40], experience with the SW potential indicates that it is a reasonable representation of silicon for the study of ion beam processing. This potential gives an accurate represen-

tation of many of the properties of bulk silicon, including a good description of its energy–volume relationship and of its melting behavior [39], and of the recrystallization kinetics during fast quenching from the melt [41]. In addition, recent studies of the properties of silicon point defects and small clusters [41,42], also support the validity claim for the SW potential. Comparison to very recent density functional calculations with ab initio pseudopotentials [43,44] shows good agreement between these electronic structure methods and the simple SW potential. For example, the SW potential predicts that the $\langle 110 \rangle$ split dumbbell configuration is the low energy structure for the neutral self-interstitial [41,42]. This is in good agreement with the first principles methods [43,44] although the exact details of the configuration may be slightly different [42] from the first principle methods [44]. On the other hand, the vacancy formation energy is about 1 eV lower (2.6 eV) with the SW potential [42] than with the results of first principles calculations [44].

The value of the threshold energy for defect production, E_d, along low index crystallographic directions is known in silicon. The minimum value of E_d is known to be ≈ 15 to 20 eV [45]. Recent simulations with the Tersoff potential gave minimum values of $E_d \approx 13$ eV [46], and those with the SW potential gave results for E_d of 18 eV along [111] [47], not far from the experimental values in either case. The SW results were also in agreement with experimental values of the orientation dependence of E_d [47]. These results indicate that both the SW and Tersoff potentials are well suited to describe the low energy defect production mechanisms.

As in the case of the metals, we modified the short range repulsive interaction part of the potential to account for high energy scattering. We followed the approach of Gärtner et al. [48], and modified the SW potential for energies higher, or distances of closest approach in a two-body collision shorter, than those characteristic of threshold energy events. We spline the two body part of the SW potential to the ZBL [25]. The distances at which the two potentials are joined, as well as the form of the spline function is given by Gärtner et al. [48].

2.3. Kinetic Monte Carlo simulation method

Defect diffusion simulations during cascade annealing were performed using a variant of the KMC code, McDonalds, developed by Jaraiz et al. [49]. In a KMC simulation, the Monte Carlo steps can be related to the real time through the relationship

$$t = \frac{\delta^2}{6D}, \qquad (4)$$

where t, δ, and D are the real time, the jump distance, and the diffusivity, respectively.

The McDonalds code uses temperature dependent diffu-

sivities to calculate jump probabilities and considers the migration of point defects, clusters and impurity atoms. The code allows clustering of defects, dissociation of clusters and precipitation reactions. The code also has the capability to allow the interaction of defects with microstructure features such as dislocations and grain boundaries, but this has not yet been implemented in the current version used in this work.

Data required to carry out the kinetic Monte Carlo simulations are diffusivities of defects and impurities, spontaneous recombination volume of vacancies and interstitials, binding energy and capture radius of impurities and clusters, and the jump distance. The temperature dependence of the defect diffusivity can be written as follows:

$$D = D_0 \exp(-E_m/kT), \qquad (5)$$

where D is the defect diffusivity, D_0 is the pre-exponential factor, E_m is the migration energy, T is the temperature of the crystal, and k is Boltzmann's constant. For metals, the values of E_m for interstitials and vacancies are well known from experiments, but the values of E_m for small clusters and glissile dislocation loops and of D_0 for all kinds of defects have not been obtained experimentally. In silicon, the situation is much worse. The equilibrium concentrations and migration enthalpies of the vacancy and the interstitial are not known. In the following, we present results of MD calculations to obtain these values as well as the values of the binding energies of defect clusters. The capture radius and the jump distance are taken to be equal to the second nearest neighbor distance in this study.

3. Results

3.1. Molecular dynamics simulations of displacement cascades

3.1.1. Gold

Several snapshots of a 10 keV cascade in Au at 50 K are displayed in Fig. 1. Notice that the final shape of the cascade is already reached at 0.4 ps. At that point, the onset of the formation of the first cluster is clearly observed, as well as the beginning of the replacement collision sequences (RCSs). The maximum volume of the cascade is reached at about 2 ps. At 27 ps one can consider that the cascade has terminated, this value being the maximum time reached in our MD study. The final number of Frenkel pairs is 66, i.e. 66% of the prediction of the NRT collisional model with a 40 eV average threshold displacement energy. More importantly, 62 of them are in clusters. As is expected in metals, the vacancies are distributed in the central core of the cascade while the interstitials are located in the outer part. Most of the vacancies (55) form one big cluster. We also observe a trend in this cluster to evolve to a dislocation loop. The sizes of the interstitial

clusters are variable (34, 20, 8). The smallest cluster forms a prismatic dislocation loop and the larger ones exhibit the same tendency as the vacancies. These results are consistent with the simulations of Ghaly and Averback who also observed the production of vacancy and interstitial clusters in 10 keV cascades in Au [34]. Fig. 2 shows the final defect configuration generated by another 10 keV cascade at 300 K. In this case, no clusters are observed and the defect production efficiency is only 6% of the NRT prediction. All the interstitials are ejected by RCSs. In Fig. 3, we show the primary damage state at 60 ps resulting from a 30 keV cascade at 300 K. Here, the defect production efficiency is 30% of NRT (112 Frenkel pairs) and about

70% of the defects are in clusters. About 70 vacancies are clustered in two Frank loops. Only nine interstitials remain as single type and only two as di-interstitials. The rest are present in four clusters of sizes 36, 33, 25 and 7.

In order to understand the production of defect clusters and the difference in behavior between the two 10 keV cascades of Figs. 1 and 2, it is illustrative to consider the details of the cascade evolution. Fig. 4a–d show the hydrostatic and shear pressure profiles calculated for both 10 keV cascades as a function of distance from the centroid of energy distribution of each cascade. Pressures are calculated at the atomic level according to the formulation of Vitek and Egami [50]. At short times (around 0.2 ps),
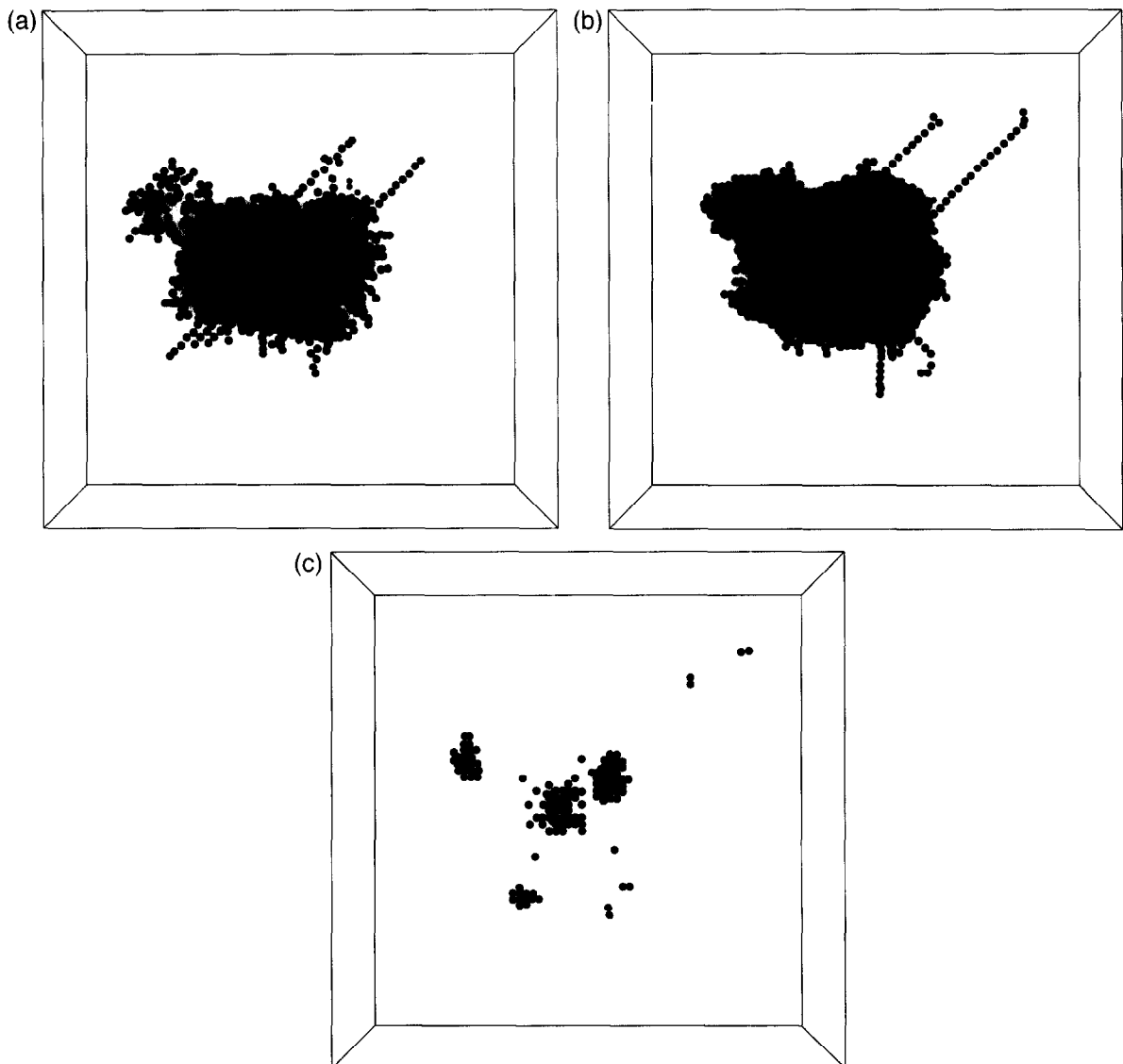

Fig. 1. Snapshots of a 10 keV cascade in Au at 50 K (a) after 0.4 ps, (b) 2.0 ps and (c) 27 ps. Both interstitials (dark circles) and vacancies (light circles) are in clusters.
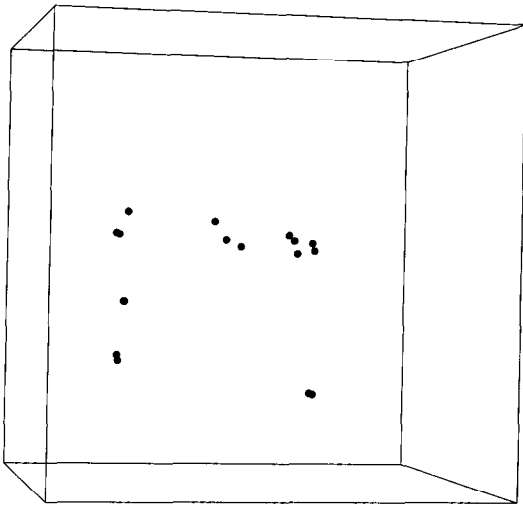
Fig. 2. Defect configuration from a 10 keV cascade in Au in which no clusters are formed.

when the cluster formation is about to take place, the pressure generated in the first cascade is much higher than in the second one. The extremely large values of the pressures are due to the fact that the calculations are carried out by considering the volume derivatives of the energy of each atom. Thus, the results are skewed by the fact that during these early times, the region is not yet thermalized and many atoms have very high kinetic energies and are in close proximity to other atoms. Nevertheless, the results show that the distribution of collision events during the very early stages of the cascade and the establishment of extremely high pressure gradients as a result of localized high energy collisions are responsible for the setting up the conditions for both vacancy and interstitial clustering. Note also that as shown in Fig. 1 the interstitial clusters are ejected at about the same time as the RCSs. Concomitant with the high pressures established in the cascade region there is a drastic reduction in the atomic density. Again, for the cascade that results in defect clustering, the density reduction at early times is much larger than for the cascade that does not produce clusters. It is also interesting to note that no significant difference in the temperature profiles for these two cascades were observed at any time.

3.1.2. Vanadium

MD simulations of displacement cascades in vanadium at 10 K for 1, 2, and 5 keV recoils were carried out by Morishita and Diaz de la Rubia [37]. The results show that the defect production efficiency is 55% for these cascades when using a 40 eV average threshold displacement energy as suggested by the ASM standards [51]. The defect production efficiencies obtained for bcc vanadium are lower than those for other fcc metals such as Cu or Au. The defect clustering efficiencies are also much lower than

for fcc metals and are similar to those obtained in bcc iron by Phythian et al. [52] and Bacon et al. [53]. Fig. 5 shows the cluster size distribution obtained in these simulations. No clusters larger than 2 vacancies or four interstitials were observed even at 5 keV. This suggests that defect cluster formation in cascades is greatly influenced by lattice type and seems to be consistent with experimental observations of lower probability of cascade collapse in bcc metals than in fcc metals [54].

3.1.3. BCC iron

We have recently carried out extensive simulations of the primary damage state in Fe as a function of recoil energy. The simulations were performed at 600 K for primary knock-on atom (PKA) recoil energies ranging from 100 eV to 20 keV. According to calculations using the SPECTER code [55], 60% of the PKA atoms produced by fission neutron irradiation of α-Fe have energies less than 20 keV. Thus, the range of PKA energies used in this study represents a reasonable approximation for describing irradiation by fission neutrons. Moreover, as recently demonstrated by Stoller et al. [56] higher energy cascades may be expected to break up into subcascades.

Fig. 6 shows a comparison of typical defect configurations produced by 5 and 20 keV displacement cascades 10 ps after the initiation of the recoil. Pairs of open circles are interstitial dumbbells, and small dots are vacancies. Fifteen Frenkel pairs are generated in this 5 keV cascade simulation. Vacancies are located in the center region of the cascade, while isolated $\langle 110 \rangle$ interstitial dumbbells produced by RCSs can be found in the periphery. Two di-interstitials were also formed. On the other hand, the 20 keV cascade shown in Fig. 6(b) generated 55 Frenkel pairs. Many mono-interstitial dumbbells are located at the edge of the cascade region, but large interstitial clusters are also present.
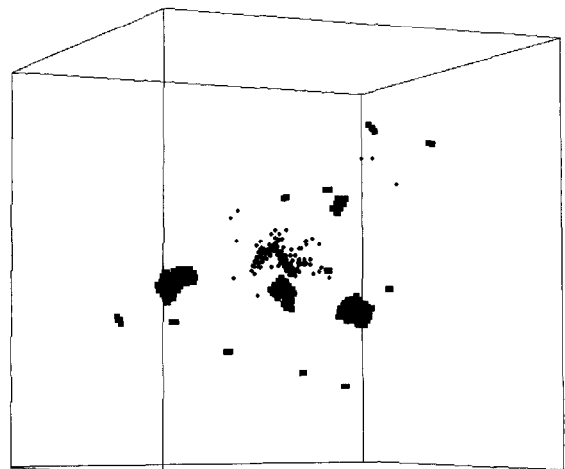

Fig. 3. Primary damage state from a 30 keV cascade in Au. The majority of the vacancies and the interstitials are in clusters.

Detailed analysis of the cascade evolution process shows that these large interstitial clusters are formed at the interface of local subcascades. This can be explained as follows. Fig. 7(a) shows the damage configuration at 0.1 ps, including lattice sites where atomic replacements have taken place. The arrow in the figure indicates the original location of the PKA, and the cascade primarily grows toward the bottom of the computational box in this case. The figure shows that there are almost five local subcascade regions labeled A to E. These subcascades merge at 0.49 ps as shown in Fig. 7(b), but the comparison between Fig. 6(b) and Fig. 7(a) indicates that the large cluster is

formed at the interface of subcascades B and D. Similarly, the clusters at the top and bottom of the cascade region are also formed at the interfaces of the subcascades A and B and D and E, respectively. In each subcascade, vacancies are produced at the center area, while interstitials are produced at the edge of the subcascade region.

More detailed analysis of the formation process of the largest interstitial cluster is also interesting. Fig. 8(a)–(d) are close-ups of the center region of the cascade. At 7.9 ps, there are three medium size interstitial clusters labeled as A to C. Cluster C is sessile. However, the other two, A and B, are mobile and merge into one larger cluster at 8.0 ps.
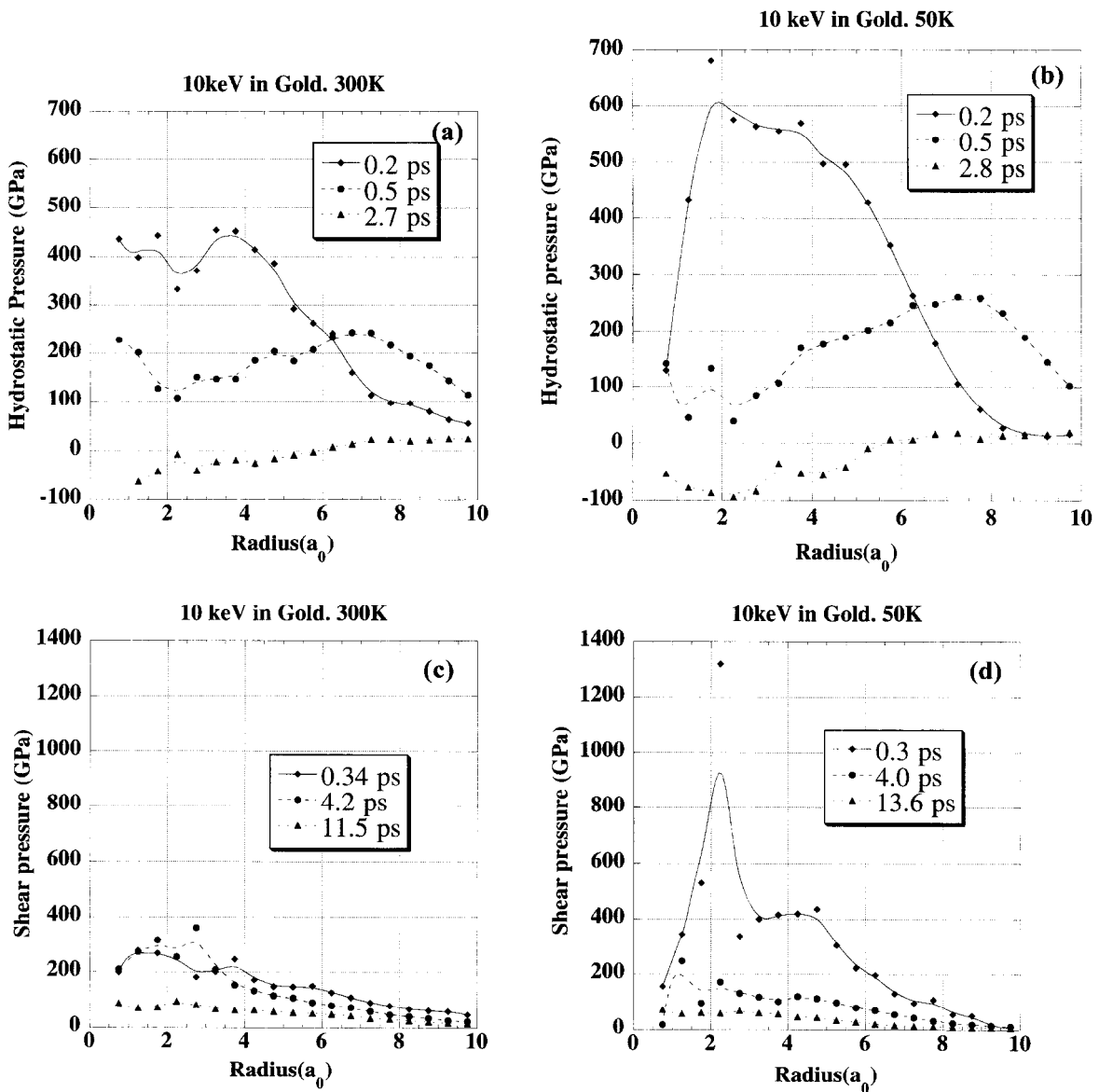

Fig. 4. Hydrostatic and shear pressure profiles in 10 keV gold cascades in gold. The peak values for the cascade with clusters formation (b) and (d) are much higher than those of the cascade without clusters (a) and (c).
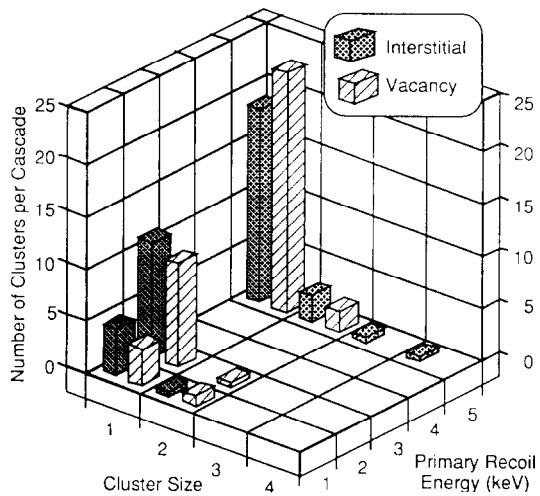
Fig. 5. Cluster size distribution for a vanadium cascade.

This newly formed cluster is also mobile, and migrates toward cluster C at 8.5 ps to form the final large cluster as shown in the figure at $t = 9.5$ ps. Notice that while the single interstitials appear to be nearby the loop in these projections, this is in fact not the case and they do not move in the time scale (1.5 ps) of the loop formation process.

Vacancy clusters were not formed in any of the displacement cascade simulations carried out in these studies. This is in sharp contrast to other cascade simulations in fcc metals such as Cu and Au [32,57], where vacancy dislocation loops are often formed in the center region of the cascade, but agrees well with simulations in other bcc metals such as V where no evidence for vacancy clusters was found either [37].

The number and size of interstitial clusters produced by different PKA energies at 10 ps after cascade initiation are summarized in Fig. 9. Interstitial clusters having more than five dumbbells are formed for cascades with PKA energies larger than 5 keV, and large clusters with more than ten members are formed for PKA energies greater than 10 keV. These results are also in good agreement with previous studies by other authors [56].

The defect production efficiency, i.e., the number of Frenkel pairs normalized by the number calculated by the modified Kinchin–Pease (or NRT) model [4] is plotted in Fig. 10 as a function of PKA energy. For very low PKA energies such as 100 and 200 eV, the results agree well with the NRT model. For higher PKA energies, however, the NRT model clearly overestimates the number of Frenkel pairs. In the 20 keV recoil events, the defect production efficiency is only 30% of the NRT model, which is consistent with experimental studies in Cu and Ag [3] and with previous MD simulations in many metals for PKA energies up to 25 keV [2,51,58,59]. Note that these results are based on the number of defects at 10 ps after event

initiation. In order to calculate the fraction of freely migrating defects at elevated temperature, we need to consider how many of these defects undergo recombination within their nascent cascade and how many are able to escape. This issue is addressed in the next section.

3.1.4. Silicon

The primary damage state in a silicon crystal following 3 keV B and 15 keV As cascades is shown in Fig. 11(a) and (b), respectively. In units of reduced energy [60], these PKAs correspond to 0.3 and 0.07. However, because of the different ion masses, the projected range of these PKAs is similar. Fig. 11 shows the distribution of atoms with
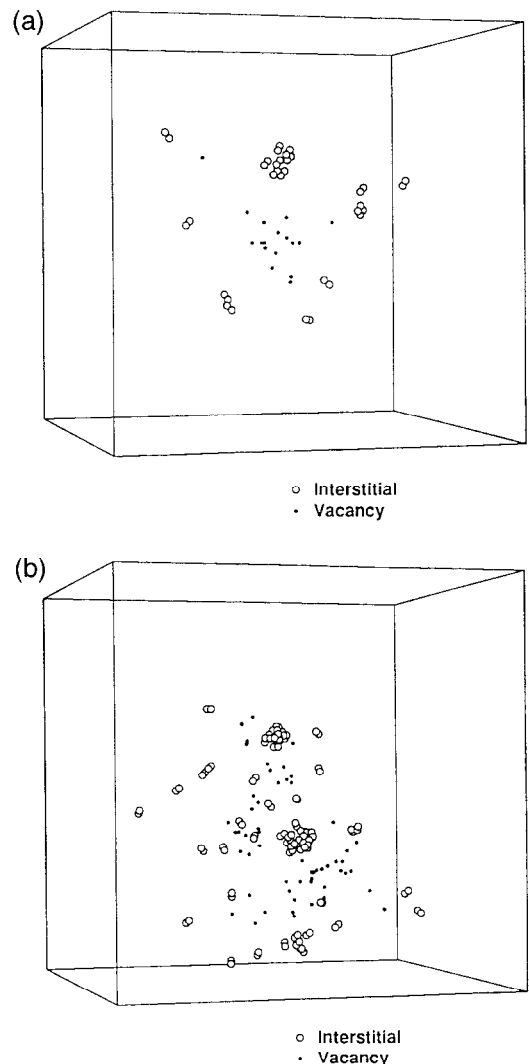

Fig. 6. Primary damage state at 10 ps for (a) 5 keV and (b) 20 keV cascades, respectively. Open circles are interstitials and small dots are vacancies. For the 5 keV case, vacancies located in the center region are surrounded mostly by mono-interstitials. On the other hand, for the 20 keV cascade, large interstitial clusters form.

(a) 0.10 psec

PKA
location   A

B

D

C

E

○ Interstitial
⊙ Replaced atom
· Vacancy

(b) 0.49 psec

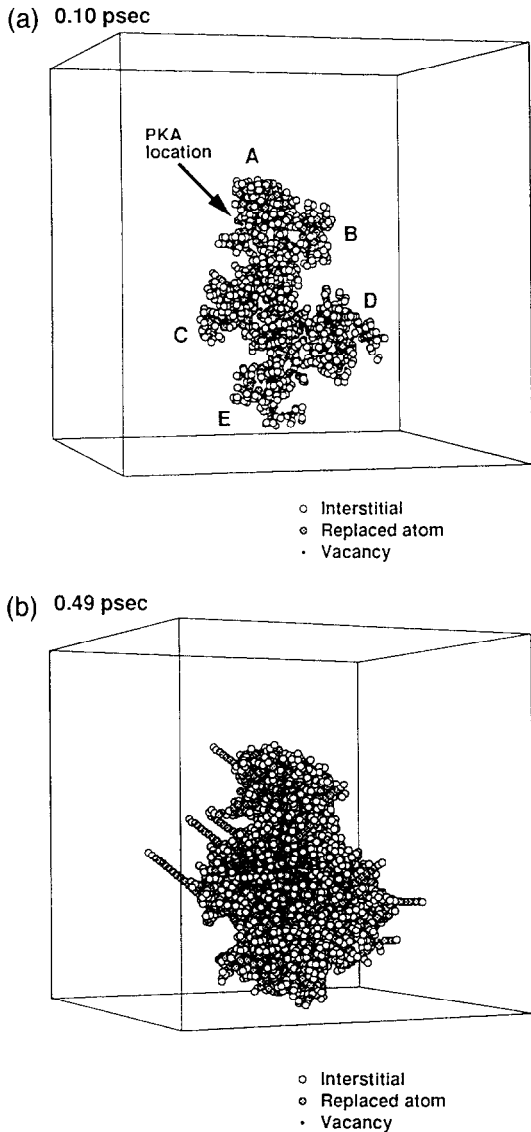○ Interstitial
⊙ Replaced atom
· Vacancy

Fig. 7. (a) Damage configuration at 0.1 ps for the 20 keV cascade in (b). The tip of the arrow indicated the initial position of the PKA. The labels A–E correspond to five distinct, albeit connected, subcascade regions. (b) At 0.49 ps the cascade reaches its maximum extent and all the subcascades have overlapped. RCSs are clearly seen emanating from the cascade.

potential energy above the ground state of a silicon crystal 10 ps after the initiation of the PKA above the (001) surface plane. At this time, the energy deposited in the crystal by the PKA has been dissipated by the damped periodic boundaries. The gray scale represents atomic level stress, σ, where $\sigma = \Omega^{-1}\partial V(\zeta r_{ij})/\partial \zeta$, Ω is the atomic volume of the crystal, and ζ is a distance scaling factor. Lighter tones indicate tensile stress and darker ones compressive stress. For the point defects, tensile stress indicates vacancies, and compressive stress indicates interstitials. For example, four neighboring atoms under tensile stress in the figure correspond to an isolated vacancy. For the large clusters of disordered material, the average hydrostatic stress is nearly neutral [61]. The number of atoms, N_p, with $E_p > 0.2$ eV is 230 and 1899 for the 3 keV B and the 15 keV As cases, respectively. Clearly seen in these figures is the fact that while 15 keV As cascades result in large clusters of these disordered atoms, both the number and size of the disordered atom clusters produced by the 3 keV B cascade is much smaller.

The nature of the physical processes that give rise to this primary damage state was analyzed by Diaz de la Rubia and Gilmer [61] for 5 keV Si PKAs in Si. The results showed that the structure of the material in a cascade region changes dramatically during the period of the simulation. Fig. 12 shows the radial distribution function (rdf) at four different times for a region in the core of the cascade such as the one in Fig. 11(b). The structure shown in Fig. 12(a), corresponding to 1.1 ps, is similar to that of bulk liquid silicon at the melting point, Fig. 12(c), although the peaks are broadened and less distinct in the case of the cascade. The final structure at 7 ps, Fig. 12(b), is similar to that obtained for bulk amorphous SW silicon, in the case were the liquid is cooled from the melting point to 0 K in 5 ps, Fig. 12(d). Note the presence in both cases of a peak at 3.4 Å, corresponding to the shoulder that is usually observed for amorphous SW silicon at finite temperatures [62–64]. In Fig. 12(e) we show the rdf for a liquid quenched at a rate two orders of magnitude slower, i.e. in 500 ps. The rdf from the slower quench exhibits a peak at 3.4 Å that is much reduced in height. This comparison with the structure of the quenched liquid indicates that the amorphous material in this region has a structure that is determined by the fast quench of the liquid-like cascade

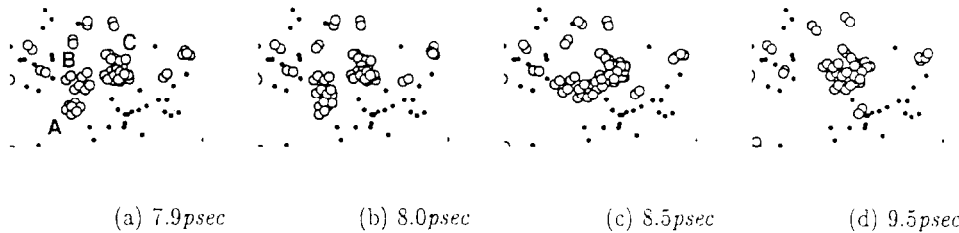(a) 7.9psec   (b) 8.0psec   (c) 8.5psec   (d) 9.5psec

Fig. 8. The formation process of the large interstitial cluster for the 20 keV cascade in Fig. 7(b) is shown in this series of close-up views. Three medium size clusters can be seen at 7.9 ps. Two of them are glissile and agglomerate immediately. By 9.5 ps the large local stresses in this region have resulted in the formation of a single cluster.
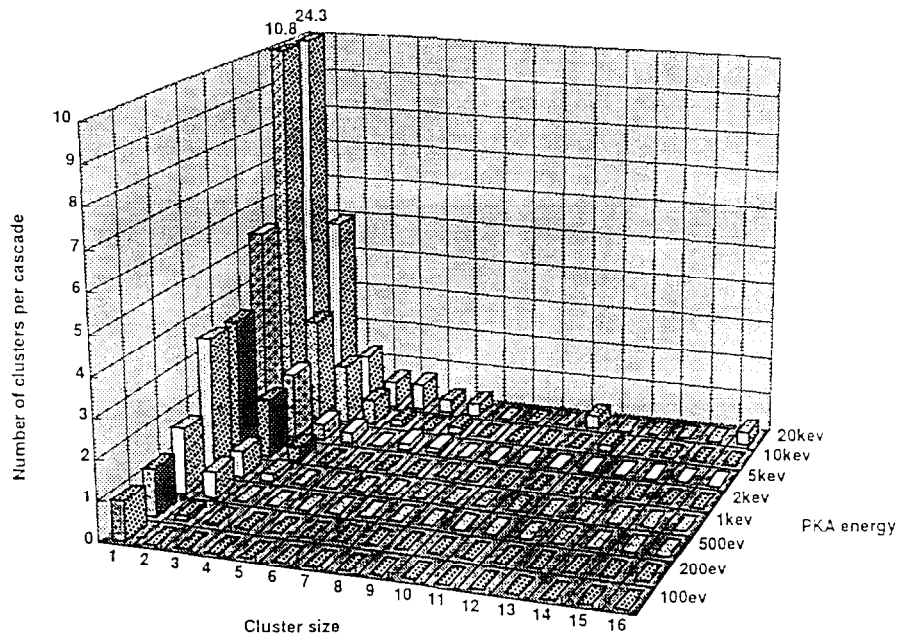
Fig. 9. Number of interstitial clusters per cascade as a function of clusters size and PKA energy. Large clusters with more than ten interstitial dumbbells are produced in cascades with more than 10 keV recoil energy.

region by the conduction of heat to the surrounding crystal. The average coordination number in this region, as determined from the integral of $g(r)$ out to the first minimum, was found to increase to a value of ≈ 6.5 at 0.5 ps and decrease to ≈ 4.3 after equilibration with the surrounding

lattice. Similarly, the density in the region initially decreases to a value 10% smaller than the crystalline density and then changes to a value slightly larger ($\approx 3\%$) than the equilibrium density at ≈ 0.5 ps. At early times, due to the energetic collisions the average atomic stress increases to a
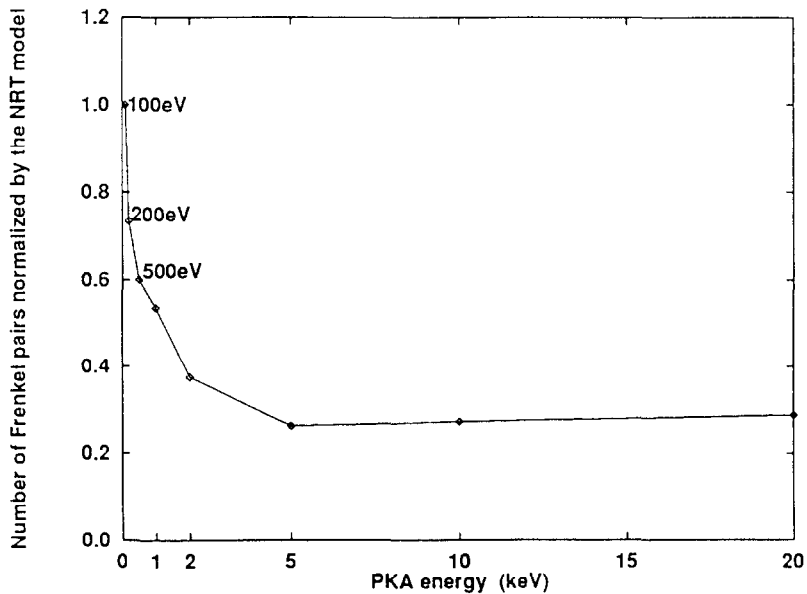

Fig. 10. Defect production in cascades as a function of recoil energy normalized to he prediction of the NRT model. At energies above 5 keV the defect production efficiency is 30% relative to the dpa standard.

compressive value of 10^{12} dyne/cm^2, and then changes sign to tensile stress at about 0.5 ps, consistent with the density and coordination number changes described above.

We have also shown in another work that the disordered zones produced by 5 keV Si cascades in Si appear to be amorphous in nature [61]. This conclusion was based on analysis of the pair correlation function of the disordered zones, and on the fact that solidification of the locally molten cascade zone occurs at a rate $\approx 10^{-4}-10^{15}$ K/s which in Si leads to interface velocities much larger than the critical velocity for amorphization [65]. We have also introduced a criterion based on the time averaged distribution of bond angles for the atoms in the cascade region. When performing a time average of the bond angle distribution sustended by an atom and its neighbors, the distribution becomes narrower for a crystalline sample, but remains invariant for an amorphous network. This difference in behavior, illustrated in Fig. 13, allows the introduction of the following criterion: if after the time average a silicon atom is fourfold coordinated and the six possible angles that it forms with its neighbors fall within the limits of the averaged distribution during the same time for a perfect crystal, the atom is considered as a crystalline. Conversely, if this condition is not fulfilled, the atom is

considered as part of an amorphous network. A more detailed description of the method and a comparison with criteria proposed by other authors has been given elsewhere [66]. Applying this criterion to the center of a highly damaged region such as that shown in Fig. 11(b), we observe that 95% of the atoms are amorphous. Thus, we will refer to the large disordered zones, particularly those produced by high mass ions such as As, as amorphous pockets throughout the rest of this paper.

The results of these MD simulations provide insight into the defect production process in silicon. One of the most striking results of this work is the fact that very few isolated Frenkel pairs are produced directly by the displacement cascades. This can be understood by considering that isolated point defects are produced in cascades by replacement collision sequences along low index crystallographic directions [67]. As we have recently shown, such RCSs in silicon are extremely short, two to three atomic replacements long at most [68]. Therefore, the probability of such an RCS producing a stable (i.e., separated beyond its own spontaneous recombination volume) vacancy–interstitial pair during a keV cascade is very small. Our simulations for 5 keV Si recoils in Si resulted on an average of 1.5 isolated self-interstitials per 5 keV cascade

(a)   B (3 keV)   **(b)   As (15 keV)**
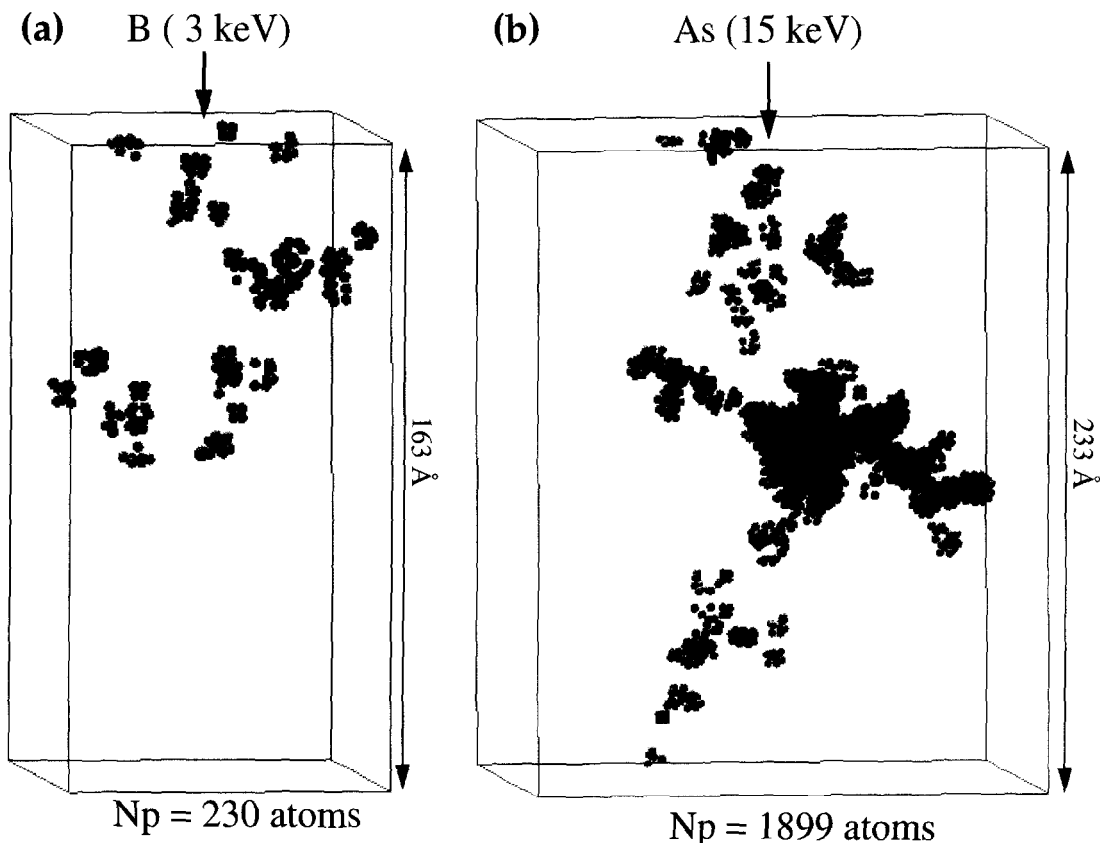
Np = 230 atoms   Np = 1899 atoms

Fig. 11. Atoms with potential energy higher than 0.2 eV for 3 keV B (a) and 15 keV As (b) implantation in Si at 300 K after 10 ps.
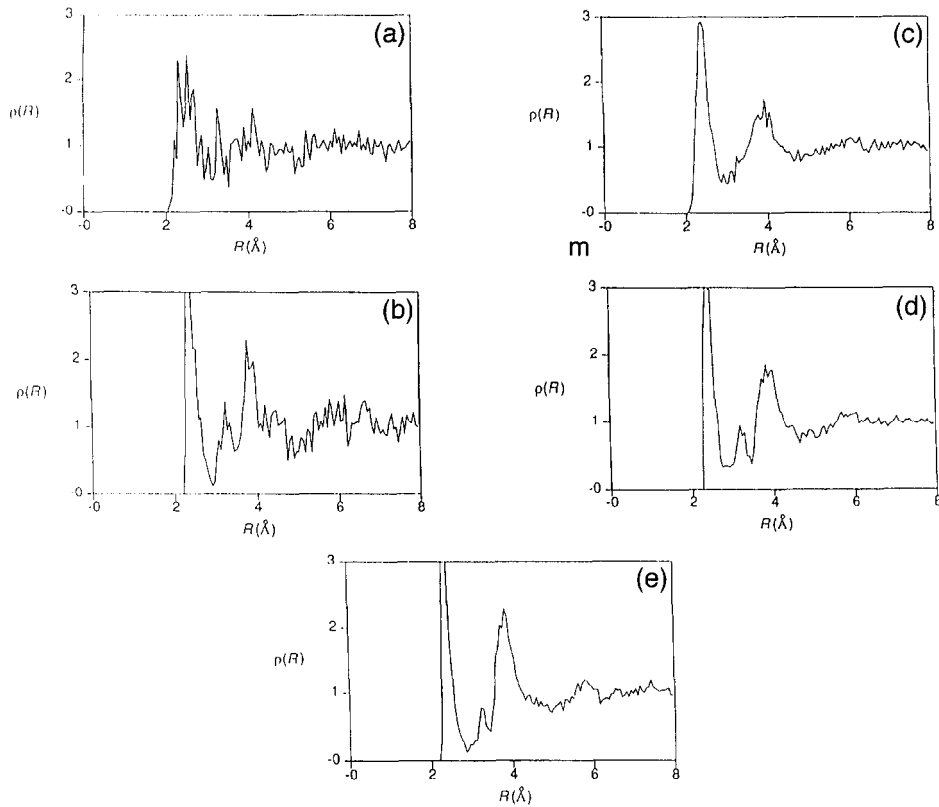
Fig. 12. The radial distribution function (rdf) of atoms in a cascade region ((a) corresponds to 1.1 ps and (b) to 8 ps) are compared with those of bulk silicon. (c) is the rdf for liquid silicon at the melting point, (d) is the rdf for amorphous silicon quenched form the melt in 5 ps, and (e) is the rdf from amorphous silicon quenched from the melt in 500 ps.

and 0.5 vacancies. These numbers are about two orders of magnitude smaller than the number of displacements predicted by binary collision approximation (BCA) models such as the modified Kinchin–Pease expression of Sig-
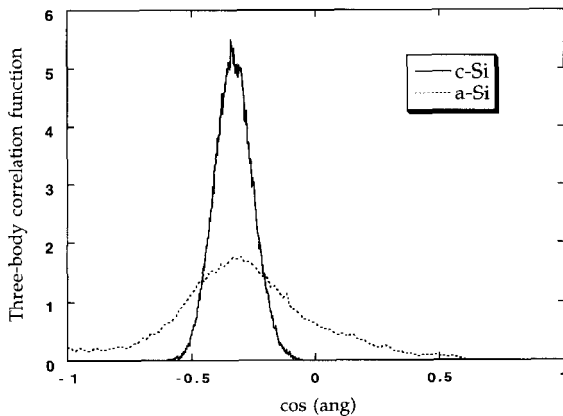

Fig. 13. Three-body correlation functions for crystalline and amorphous silicon at 773 K. In both cases the distributions are peaked around the same value, 109.5°, the basic angle in the diamond structure.

mund [69]. For a damage energy of 5 keV and a threshold displacement energy, E_d, of 15 eV, 133 point defects are predicted. On the other hand, large pockets of unrelaxed amorphous material are produced by the displacement cascades. For these 5 keV cascades, the disordered regions contain an average of ≈ 800 atoms; i.e., seven times the number predicted by the BCA calculations.

It is also of interest to analyze the way in which the damage distribution and morphology change as the implantation energy increases. As the ion energy increases, not only does the total amount of damage, as expected, but the size of the largest amorphous pocket increases as well. Fig. 14(a) shows the total number of interstitials, or displaced atoms, and the total number of isolated, mobile interstitials, as a function of recoil damage energy for As cascades. The total number of displaced atoms increases linearly with energy. As we will discuss in more detail below, the slope of this curve, $s_{As} = 55$ keV^{-1}, is approximately twice what would be predicted by BCA models, $s_{BCA} = 0.8/2E_d = 27$ keV^{-1}. The fraction of mobile interstitials also increases with recoil energy, but with a different slope $s_m \approx 5$ keV^{-1}. For boron, Fig. 14(b) shows the displaced atom and mobile defect production vs. damage energy for 1 keV, 2 keV, and 3 keV displacement

cascades. In contrast to the As case, the slope of the displacement production curve is $s_B = 31$ keV^{-1}, which is basically equal to the prediction of the BCA calculations. Also, the efficiency of mobile defect production for B cascades is 11 keV^{-1} in contrast to 5 keV^{-1} for the As results presented above.

Because of the energetic collisions and the density changes induced by the incoming particle, the amorphous regions produced by cascades in silicon frequently have densities that differ from that of the crystal. Also, because of their large surface-to-volume ratio and the fact that they are surrounded by crystalline material, these amorphous pockets are highly unstable, and recrystallize at much

lower temperatures than a stable planar amorphous/crystal interface. Upon annealing for several picoseconds at elevated temperature, such density fluctuations result in the appearance of vacancies and self-interstitial atoms in the recrystallized material. This process is illustrated in Fig. 15. In Fig. 15(a), we select a region where amorphous material has been produced as a result of a 5 keV cascade. Upon annealing for 1 ns at 1300 K, Fig. 15(b) shows that the amorphous material has recrystallized and a distribution of monovacancies (3), vacancy clusters (1 divacancy) and ⟨110⟩ dumbbell self-interstitials (2) are present. Note that out of approximately 500 atoms originally present in the annealed amorphous pocket, only two new self-intersti-
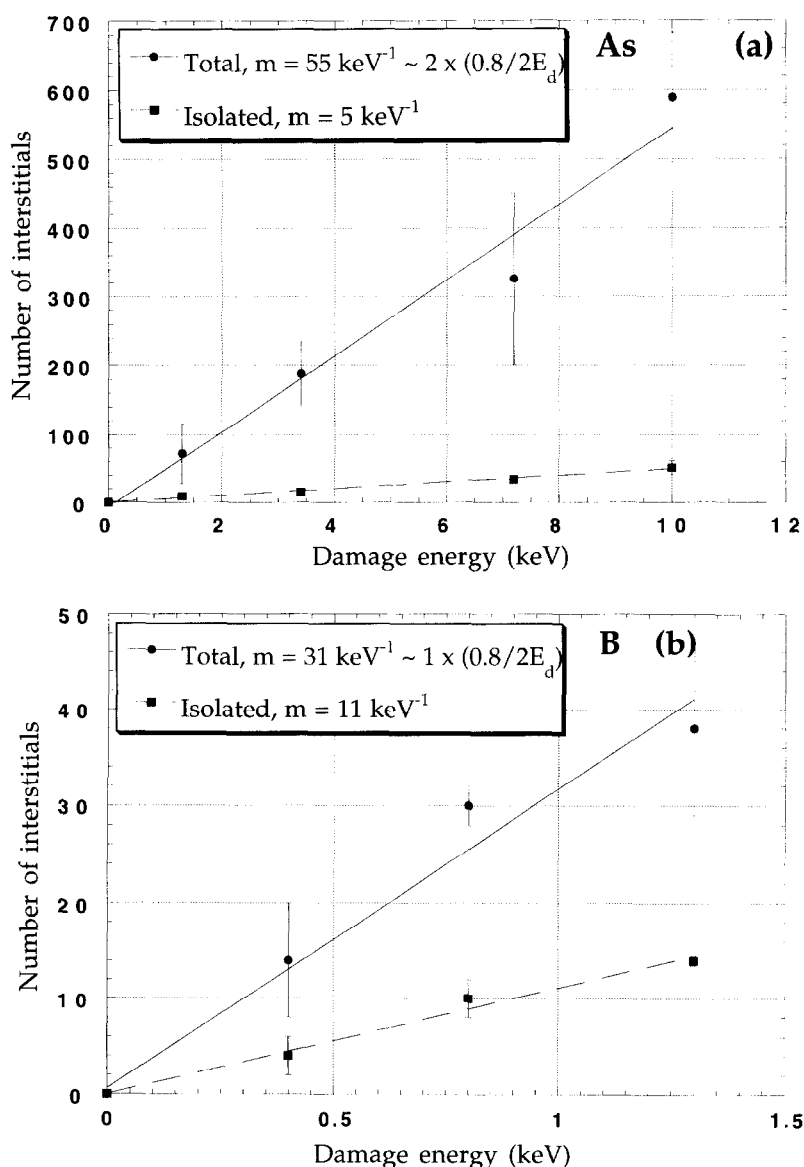

Fig. 14. Total number of displaced atoms and total number of mobile interstitials as a function of the damage energy for As (a) and B (b) implantation in silicon.

tials, one monovacancy, two di-vacancies, and a tri-vacancy remain as damage.

These results help explain many experimental observations of intrinsic dislocation (interstitial type) loop growth during annealing of silicon following implantation. Schreutelkamp et al. [70] have shown that implantation with low energy ions in silicon can result in dislocation loop formation during subsequent annealing at 900°C if the number of displaced atoms exceeds a critical value. However, their RBS/channeling measurements showed that for 100 keV irradiation of silicon with P + , only about 0.07% of displaced atoms end up in the loops. This is consistent with our observation that displacement cascades produce large amorphous pockets and few isolated, freely migrating defects. As we have shown above, when the amorphous pockets recrystallize during annealing point defects and defect clusters appear in the lattice. Nevertheless, their number is only a small fraction, approximately 1% or less, of the number of atoms originally present in the amorphous pockets.

3.2. Kinetic Monte Carlo simulations of defect annealing

3.2.1. FCC metals

During irradiation at temperatures where some or all of the defects produced by the displacement cascade are mobile, changes in microstructure and mechanical properties ensue. A key requirement in modeling these changes is understanding and being able to predict how many of the defects produced can escape their nascent cascade to migrate through the lattice and modify the microstructure. KMC simulations have been used for this purpose since the early 1970s. However, their use has not been extensive, mainly due to the lack of accurate information on the kinetics and energetics of the point defects and the defect clusters. More recently, Heinisch [71] has combined the results of our own MD simulations of high energy displacement cascades in Cu with data on defect diffusion

and defect cluster binding energies also obtained from MD to investigate the number of defects that escape their cascade as a function of annealing temperature. In the following, we present results of our calculations of defect kinetics and annealing from displacement cascades in fcc metals and Si.

In order to investigate the fraction of defects produced by a cascade such as that of Fig. 3 that can escape recombination and migrate long distances, information is needed on the prefactor and activation energy for migration of the various defects, including the clusters, as well as on the binding energy of the defect clusters. The first quantities determine the rate of hopping and enter the KMC simulations through the Boltzmann factor that determines how often a particular class of defect is picked to make a diffusion jump. The binding energies determine the stability regime of the various clusters and therefore whether a particular cluster will shrink by emission of point defects during the anneal or not. Note that in these KMC simulations, all cluster sizes can be treated and no assumptions regarding an average cluster size need to be made. Also, it is interesting to note that in KMC simulations defect diffusion can occur in any number of dimensions and is not limited to a three-dimensional random walk. Therefore, one-dimensional glide of small interstitial loops can be incorporated trivially into the simulations and taken into account. Basically, no homogenization assumptions need to be made in KMC simulations.

The binding energies of vacancy clusters can be calculated from MD simulations. The binding energy, $E_b^\alpha(n)$, of a cluster is defined as follows:

$$E_b^\alpha(n) = \left(E_f^\alpha(n-1) + E_f^\alpha(1) \right) - E_f^\alpha(n), \qquad (6)$$

where α is either i (interstitial cluster) or v (vacancy cluster). For large clusters, the calculations are too time consuming and usually the data for small clusters is extrapolated by a function that fits the small size data and takes into account the fact that at large sizes the binding energy
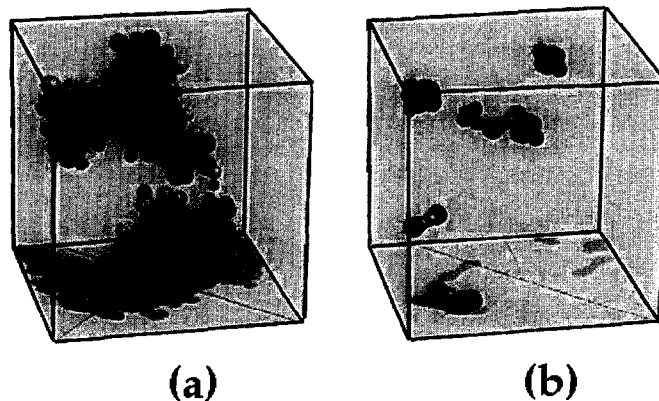

(a)   **(b)**

Fig. 15. Annealing of cascade-induced amorphous pockets by molecular dynamics. (a) State immediately after the cascade. (b) After 1 ns annealing at 1300 K the amorphous material has recrystallized and self-interstitials and vacancy clusters are left behind.

should be equivalent to the vacancy formation energy. In addition, it is generally assumed that the binding energy curve follows an $n^{2/3}$ relation. For example, for the binding energies of larger clusters, we obtained the following expression for Pb:

$$E_b^v(n) = 0.5 - 0.58\left(n^{2/3} - (n-1)^{2/3}\right) \text{ (eV)}.7$$

In the studies presented below, the binding energies of interstitial clusters are taken to be large enough that no dissociation is allowed at the temperatures of the simulations.

Using MD simulations, we have also calculated the diffusivities of the mono-vacancy, the mono-interstitial, and the di-, and tri-interstitial clusters in Pb and Au. Details of the diffusivity calculations will be given elsewhere [23]. The extracted activation energies for interstitial

and vacancy diffusion are 0.02 and 0.45 eV, respectively in Pb, and 0.03 and 1.0 eV, respectively in Au, which agree with experimental data [72,73] except for the interstitial in Au for which no value for activation energy has been determined from experiments. Nevertheless, the calculated value of the activation energy for migration is very low, which is consistent with experiments.

It is also interesting to note that both the di- and tri-interstitials execute basically a one-dimensional random walk on a (111) plane along the ⟨111⟩ direction, but with sporadic changes in direction to another ⟨110⟩. More details of these simulations will also be presented in a future publication. Nevertheless, it is clear from the present studies that, in modeling damage evolution, this one-dimensional migration behavior must be taken into consideration.
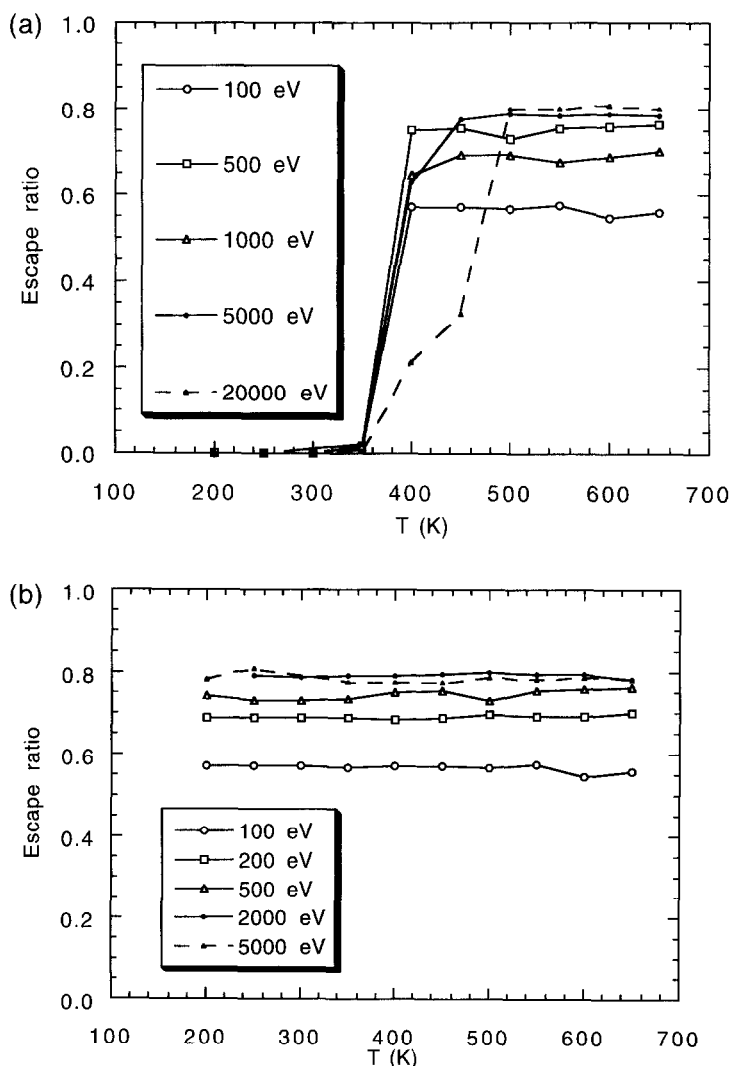

Fig. 16. (a) Fraction of vacancies that escape their nascent cascade in Au as a function of temperature for different coil energies. (b) Same but for interstitials.

Using the results of the MD simulations of cascades and defect kinetics described above, we have recently calculated the escape probability of defects from cascades in Pb and Au as a function of temperature and recoil energy [23]. The size of the KMC computation box is 100^3 nm^3. For a given PKA energy, the starting defect microstructure is introduced at the center of the KMC computation box according to the spatial configuration obtained by the MD simulations of the corresponding displacement cascade. Then, the system is annealed for a given time period at a given temperature, and the number of defects that are able to reach the edges of the KMC computational box are counted to determine the escape fraction. We define as the escape ratio the number of defects that reach the KMC box edge divided by the initial number of defects (i.e. number of defects at 10 ps in the MD simulation), and as the FMD production efficiency, η, the number of escaping defects divided by the total number of defects predicted by the NRT model. As described in Section 2, the KMC simulations consider defect diffusion, clustering, and annihilation and dissociation of point defects and their clusters. Once a defect reaches the surface of the KMC computational box, it is deleted from the active defect list, and its migration is no longer traced. Since we use a series of random numbers to simulate the diffusion and interaction of the defects in the box, the results are dependent on the random numbers used. Therefore, to improve the statistics, we performed 100 annealing runs for each of the PKA energies simulated by MD using a different series of random numbers and then calculated the average escape ratio for each PKA energy. For example, for 5 keV PKAs, we did 700 (7 × 100) simulations to calculate the escape and FMD production efficiencies.

For the simulations presented here, the time period of annealing was chosen to be 1000 s. As explained above, we consider clusters that contain between 3 and 10 interstitials to execute a one-dimensional random walk. This is
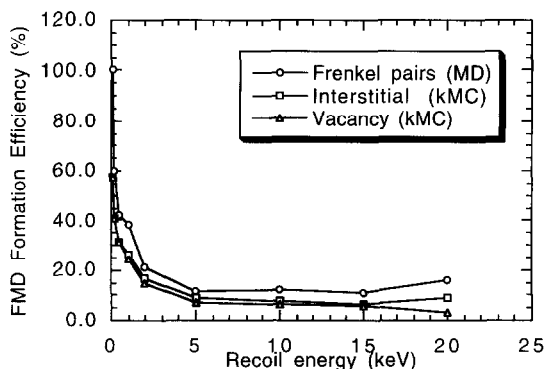

Fig. 17. The production of freely migrating defects as a function of the recoil energy normalized to the NRT standard. Also included for comparison are the results for the as-produced defects in the cascade.

Table 1
Energies for boron clusters as obtained from ab initio plane wave pseudopotential calculations and used in the Monte Carlo simulations of B diffusion in silicon reported in this paper

Reaction	Energy (eV)
Bi + Bs − B2I	0.85
Bi + B2I − B3I2	0.33
B3 + I − B3I	3.31
B3I + Bi − B4I2	1.52

consistent with the ideas of Trinkhaus et al. [74,75], who have reported that small interstitial clusters can unfault to form glissile dislocation loops and therefore migrate in one dimension.

Fig. 16 shows the escape ratio obtained from our simulations as a function of the PKA energies. Vacancy clusters dissociate between 350 and 500 K, and below this temperature a marked assymetry in the escape probability of interstitials and vacancies is 0 below 350 K and that of escaping interstitials is 80% for 5 keV recoils and above. For recoil energies less above 5 keV, the escape ratios of vacancies and interstitials are both more than 80%. This value decreases to about 60% as the recoil energy decreases to 100 eV.

By combining the defect production efficiency numbers in Au with the results of Fig. 16, we can obtain the FMD production efficiency, η, as a function of recoil energy and temperature. Results at 650 K are shown in Fig. 17. Total FMD production efficiencies for vacancies and interstitials decrease rapidly as the recoil energy increases (see also Fig. 18), and saturate at about 20% of the NRT model predictions for the PKA energies larger than 5 keV.

3.2.2. Silicon

As discussed in Section 1, modeling and predicting the diffusion of dopants in semiconductors is a key issue for the development of ultra-shallow junctions. Very recently, a Monte Carlo simulation for boron implantation and annealing has provided excellent agreement with experimental depth concentration profiles after including an 'ad hoc' model for boron clustering [76]. Following this approach we have studied the accumulation and diffusion of boron atoms at energies of a few keV in silicon, as well as the annealing of the dopant profile at high temperatures. In our model we extract the energetics for the boron clustering from ah initio plane wave pseudopotential calculations [77] and no assumption is made regarding the maximum boron cluster size.

The energetics for the boron interaction with silicon defects has been calculated using ah initio plane wave pseudopotentials and values are reported in Ref. [77]. Since these calculations are performed for 0 K no information is obtained regarding entropy factors for the different reactions, which appear as pre-factors for the diffusion
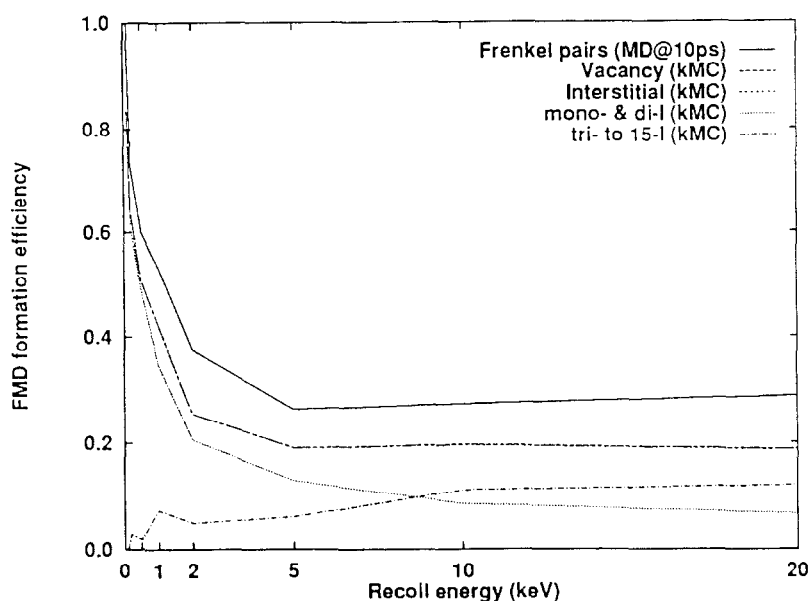
Fig. 18. The production of freely migrating defects as a function of the recoil energy normalized to the NRT standard. Also included for comparison are the results for the as-produced defects in the cascade. The freely migrating defect production efficiency in Fe is 20% at energies as high as 20 keV.

rates. These pre-factors have been fitted to experimental measurements of the boron diffusivity at different temperatures and equilibrium concentrations of silicon defects [78]. Energetics for small boron clusters including silicon self-interstitials have also been obtained by first principles calculations. In Table 1 we present the reactions between boron atoms and silicon self-interstitials that have been considered in our simulations. The diffusivities of silicon vacancies and self-interstitials (both migration energies and pre-factors), and the binding energies of clusters have been calculated using Stillinger Weber and are reported in Table 2 [42].

The as implanted profiles are obtained by coupling UT-Marlowe [79] with a kinetic Monte Carlo model. We extract from UT-Marlowe the position of the vacancies and interstitials produced by each ion, as well as the final boron location. The implanted boron is considered to be in an interstitial position (Bi) at the end of the collisional stage. Therefore, since the migration energy is only 0.3 eV, the boron interstitial is able to jump even at room temperature. Both silicon defects and boron atoms are allowed to diffuse in between two collision cascades. Consequently, dose rate effects can be directly accounted for in this model, as we already showed in previous work [80]. In Fig. 19, we present the depth concentration profile for the implantation of 500 eV B in silicon, and a dose of 10^{15} ions/cm^2, and dose rate 10^{14} ions/cm^2 s, as obtained from this kinetic Monte Carlo simulation (dots) compared to the results obtained from UT-Marlowe (solid line), where no diffusion of defects in between cascades is considered. Observe that the profiles agree for high concentration of boron atoms, however, a larger discrepancy exists in the tail of the profile. Since vacancies act as sinks for boron interstitials, the lower concentration of vacancies implies larger paths for these mobile dopants. This phenomenon of room temperature diffusion during implantation will happen in particular for low energies, when the number of defects produced per implanted ion is small. This could be an explanation for the deep tail in the concentration profiles found in some experimental mea-

Table 2

Parameters used for the Monte Carlo simulation of defect diffusion in Si. Values for diffusivities and binding energies from classical molecular dynamics calculations [42]

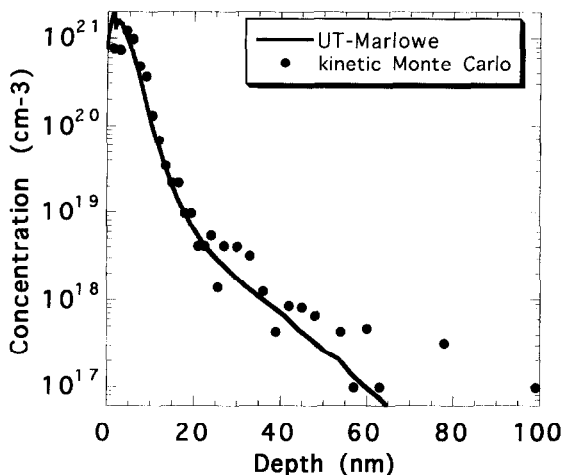|	Diffusivity (cm^2/s)	Binding energy			
		size 2 (eV)	size 3 (eV)	size 4 (eV)	size 5 (eV)
Vacancy	$0.001 \exp(-0.43/kT)$	0.62	0.78	1.2	1.82
Interstitial	$0.01 \exp(-0.9/kT)$	1.6	2.25	1.29	2.29

Fig. 19. Depth concentration profile for 500 eV B implantation in silicon at 10^{15} ions/cm^2 as obtained directly from UT-Marlowe (solid line) and as obtained from a k-MC simulation (dots).

Fig. 21. Depth concentration profile for as implanted boron and after 20 s anneal at 1000°C.

surements [81]. Note that this room temperature broadening of the dopant profile stops as soon as the ion beam is turned off.

The concentration of boron atoms in the lattice can be divided in those that are in substitutional sites (Bs), and therefore active, and those that are either in clusters or forming boron–silicon self-interstitial complexes (BI), which are also inactive and immobile. These components are represented in Fig. 20 for the case of 1 keV B implantation, at 10^{15} ions/cm^2. The percentage of each of these species with respect to the total concentration is: 21% as active, 62% as boron in clusters and 17% as boron–silicon self-interstitial complex. Therefore after the
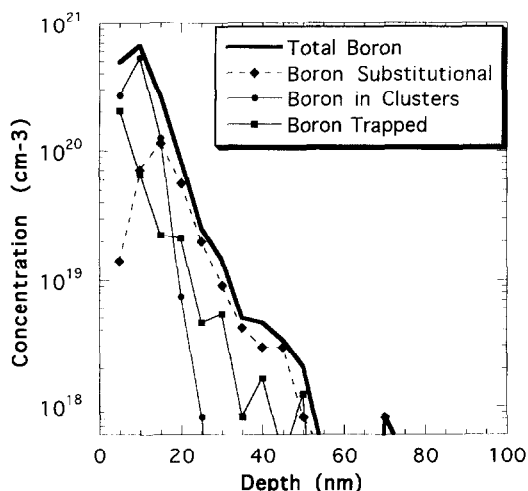

Fig. 20. Depth concentration profile for 1 keV B in silicon at 10^{15} ions/cm^2. The figure shows the boron in substitutional sites, boron in clusters and BI complex profiles after the implantation at room temperature.
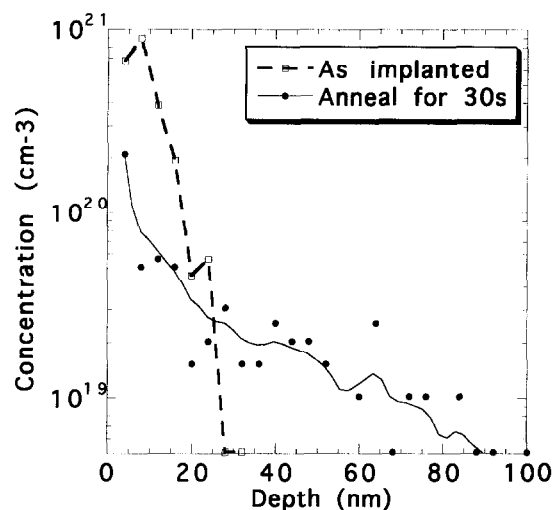
implantation most of the boron atoms are inactive and in clusters.

We have studied the evolution of the depth concentration profile of boron dopants during annealing at 1000°C. In Fig. 21 we present the initial configuration profile as well as the profile after annealing at 1000°C for 30 s, the time required to eliminate all the interstitials from the lattice and therefore reach the end of the transient. Only 0.1% of the initial interstitials remain in the lattice in the form of boron-interstitial clusters. In this case all the boron clusters have been dissolved and only those clusters including three boron atoms and one interstitial remain (see energetics in Table 1). Only 5% of the total boron concentration is in clusters.

In order to understand how the process of transient enhanced diffusion occurs we have calculated the enhancement of the boron diffusivity as a function of time during the high temperature annealing. The initial boron diffusivity is several orders of magnitude higher than the equilibrium boron diffusivity and decreases with the annealing time until all the vacancies have disappeared from the lattice. Then, the boron diffusivity increases. At the end of the diffusion process the enhancement of the diffusivity is on the order of 10, in good agreement with experimental results [82]. In Fig. 22 we show the value of the diffusion length, calculated as $\sqrt{Dt}$ where D is the boron diffusivity and t is the time, as a function of annealing time. Observe that even though the initial enhancement of the boron diffusivity is several orders of magnitude larger than in the last stage of the transient, the maximum diffusion length occurs during the second stage of the transient, due to the larger duration of this stage. In Fig. 22 we present also the average cluster size for both vacancies and interstitials. During the first stage of the transient both vacancies and
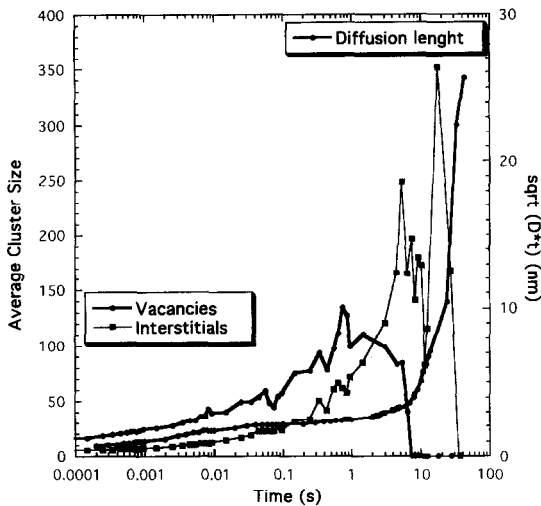
Fig. 22. Average clusters size for vacancies and interstitials (left axis) and boron diffusion length (right axis) as a function of annealing time for 1000°C.

interstitial clusters are growing in size although vacancy clusters are in average larger than interstitial ones. When all the vacancies have disappeared, interstitial clusters start growing. The total number of interstitials present after all the vacancies have disappeared is of + 1.3. It is during the growth and dissolution of interstitial clusters when the maximum diffusion length happens. The final diffusion length is of ~ 27 nm, in agreement with experimental values [82]. The active boron atoms after the first stage of the transient is of 70%. At this point, 14% of the boron atoms are still in clusters.

In conclusion, we have presented an atomistic simulation for low energy boron implantation at room temperature and high dose. We show that a small amount of the total boron concentration is active, while there is a large fraction in clusters and forming boron–silicon self-interstitial complexes, that are immobile and inactive. We have also studied the diffusion of the boron atoms during high temperature annealing and divided the transient in two separate stages. During the first stage vacancies are present in the lattice together with interstitials and the diffusion enhancement is small. The second stage starts after all the vacancies disappear and gives rise to most of the final TED.

4. Summary

In summary, we have presented a review of recent MD simulations of displacement cascades in metals and a covalent semiconductor, silicon. The results show strong differences in the nature of the primary damage state not only between the metals and silicon, but also among the various metals. For metals, cascades in Au and other noble

metals studied previously such as Cu show a strong tendency to produce highly clustered defects in the form of vacancy and interstitial prismatic and Frank loops. On the other hand, in Fe and V little evidence for vacancy clusters exists from the simulations, but small interstitial clusters appear to form at recoil energies above 5 keV. The formation of interstitial clusters directly in cascades is not yet a well understood process, but appears to be a rather universal phenomenon. In silicon, the nature of the primary damage state is very different from the case of the metals. It is composed mostly of amorphous-like pockets that form directly as a result of the fast quench of the cascade region. A significant consequence of this behavior, and of the fact that the replacement collision sequences are very short in the open diamond lattice, is the fact that very few Frenkel pair are associated with the cascades. Most of the damage is in the form of amorphous pockets.

In the second part of the paper, we have described recent attempts at modeling the fraction of defects that are able to escape their nascent cascade during irradiation or annealing at elevated temperatures. In the case of metals, these freely migrating defects are important for understanding the long time scale behavior of a material exposed to an irradiation flux at elevated temperature. We have presented results of recent kinetic Monte Carlo simulations of defect escape from cascades in Fe. Although the Monte Carlo simulation model is simple and ignores issues such as strain field effects, it appears to be a quite powerful approach for determining these important quantities. Our results show that the 1D migration of small interstitial clusters is a critical process that governs the fraction of freely migrating defects. We have shown that this fraction is of the order of 20% in Fe at 600 K. In the case of silicon, we have applied a similar kinetic Monte Carlo approach to investigate damage evolution and dopant diffusion during high temperature annealing following ion implantation. The results have shown that a combination of MD simulations, first principles calculations and kinetic Monte Carlo can be used to predict dopant profiles and transient enhanced diffusion.

References

[1] T. Diaz de la Rubia, Ann. Rev. Mater. Sci. 26 (1996) 213.
[2] D.J. Bacon, A.F. Calder, F. Gao, these Proceedings, p. 1.
[3] R. Averback, K. Merkle, R. Benedek, Phys. Rev. B 18 (1978) 4156.
[4] M.J. Norgett, M.T. Robinson, I.M. Torrens, Nucl. Eng. Design 33 (1975) 50.
[5] D.J. Bacon, T. Diaz de la Rubia, J. Nucl. Mater. 216 (1994) 275.
[6] L.E. Rhen, P.R. Okamoto, R.S. Averback, Phys. Rev. B 30 (1984) 3073.
[7] A. Muller, V. Naundorf, J. Macht, J. Appl. Phys. 64 (1988) 3445.

[8] H. Fielitz, J. Macht, V. Naundorf, H. Wollenberger, Appl. Phys. Lett. 69 (1996) 331.

[9] H. Fielitz, J. Macht, V. Naundorf, H. Wollenberger, Z. Metall. 87 (1996) 439.

[10] S.J. Zinkle, B.N. Singh, J. Nucl. Mater. 199 (1993) 173.

[11] P. Erhardt, R.S. Averback, J. Phys. F 14 (1984) 1365.

[12] The National Technology Roadmap for Semiconductors, Semiconductor Industry Association, San Jose, 1994.

[13] M. Foad, J. England, S. Moffatt, D. Armour, Ion Implantation Technology, Austin, TX, June 96.

[14] A.E. Mitchel, Nucl. Instrum. Methods B 37&38 (1989) 1160.

[15] P.M. Fahey, P.B. Griffin, J.D. Plummer, Rev. Modern Phys. 61 (1989) 289.

[16] T. Diaz de la Rubia, M.W. Guinan, J. Nucl. Mater. 174 (1990) 151.

[17] D.M. Heyes, W. Smith, in: Information Quarterly for Computer Simulation of Condensed Phases, No. 26, Science and Engineering Research Council, Daresbury Laboratory, Daresbury, Warrington WA4AD, UK, 1987, p. 68.

[18] M. Parrinello, A. Rahman, J. Appl. Phys. 52 (1981) 7182.

[19] R. Biswas, D.R. Hamann, Phys. Rev. B 34 (1986) 895.

[20] R.A. Johnson, D.J. Oh, J. Mater. Res. 4 (1989) 1195.

[21] A.M. Guellil, J.B. Adams, J. Mater. Res. 7 (1992) 639.

[22] P. Hahner, H. Stamm, European Commision Draft Report: Characterizing Materials Embrittlement: Theoretical Concepts, No. 11252-95-10, 1996.

[23] N. Soneda, T. Diaz de la Rubia, Philos. Mag. A, in press; M.J. Caturla, E. Alonso, T. Diaz de la Rubia, unpublished.

[24] S. Prönnecke, A. Caro, M. Victoria, T. Diaz de la Rubia, M.W. Guinan, J. Mater. Res. 6 (1991) 483.

[25] J.P. Biersack, J.F. Ziegler, Nucl. Instrum. Meth. 194 (1982) 93.

[26] F. Maury, M. Biget, P. Vajda, A. Lucasson, P. Lucasson, Phys. Rev. B 14 (1976) 5303.

[27] A.F. Calder, D.J. Bacon, J. Nucl. Mater. 207 (1993) 25.

[28] P. Moser, Mém. Sci. Rev. Métallurg. 63 (1966) 431.

[29] H.E. Scheafer, K. Maier, M. Weller, D. Herlach, A. Seeger, J. Diehl, Scr. Metall. 11 (1977) 803.

[30] H. Matter, J. Winter, W. Triftshäuser, Appl. Phys. 20 (1979) 135.

[31] W. Schilling, J. Nucl. Mater. 216 (1994) 45.

[32] E. Alonso, M.-J. Caturla, M. Tang, T. Diaz de la Rubia, Mater. Res. Soc. Symp. Proc. (1997) in press.

[33] S.M. Folies, M.I. Baskes, M.S. Daw, Phys. Rev. B 33 (1986) 7983.

[34] M. Ghaly, R. Averback, Nucl. Instrum. Meth. B 102 (1995) 51.

[35] H. Wollenberger, in: R.W. Cahn, P. Haasen (Eds.), Physical Metallurgy, North Holland, Amsterdam, 1983, p. 1140.

[36] R. Bortcher, W. Hertz, G. Fritsch, J.F. Watson, Proc. Int. Conf. on Fundamental Aspect of Radiation Damage in Metals, Gatlinburg, 1975, M.T. Robinson, F.W. Young, Jr. (Eds.), CONF-751006, Natl. Tech. Inf. Service, Springfield, VA 22161, p. 405.

[37] K. Morishita, T. Diaz de la Rubia, Mater. Res. Soc. Symp. Proc. 396 (1996) 39.

[38] P.E.A. Turchi, private communication.

[39] F.H. Stillinger, T.A. Weber, Phys. Rev. B 31 (1985) 5262.

[40] J. Tersoff, Phys. Rev. B 39 (1989) 5566.

[41] R.A. Brown, D. Maroudas, T. Sinno, J. Cryst. Growth 137 (1994) 12.

[42] G.H. Gilmer, T. Diaz de la Rubia, M. Jariaz, D. Stock, Nucl. Instrum. Meth. B 102 (1995) 247.

[43] P.E. Blochl, E. Smargiassi, R. Car, D.B. Laks, S.T. Pan mtelides, Phys. Rev. Lett. 70 (1993) 2435.

[44] J. Zhu, L. Yang, C. Mailhiot, T. Diaz de la Rubia, G.H. Gilmer, Nucl. Instrum. Meth. B 102 (1995) 29.

[45] J.W. Corbett, Solid State Physics, Academic Press, New York, 1972.

[46] L.A. Miller, D.J. Brice, A.K. Prinja, S.T. Picrauz, Radiat. Eff. Solids 129 (1994) 127.

[47] M.J. Caturla, T. Diaz de la Rubia, G.H. Gilmer, in: R.J. Culbertson et al. (Eds.), Materials Synthesis and Processing Using ion beams, MRS Symposia Proceedings No. 316, Materials Research Society, Pittsburgh, PA, 1994, p. 111.

[48] K. Gärtner et al., Nucl. Instrum. Meth. B 102 (1995) 183.

[49] M. Jaraiz, G.H. Gilmer, T. Diaz de la Rubia, Appl. Phys. Lett. 68 (1996) 409.

[50] V. Vitek, T. Egami, Phys. Status Solidi B 144 (1987) 145.

[51] M.J. Norgett, M.T. Robinson, I.M. Torrens, Nucl. Eng. Des. 33 (1975) 50.

[52] W.J. Phythian, R.E. Stoller, A.J.E. Foreman, A.F. Calder, D.J. Bacon, J. Nucl. Mater. 223 (1995) 245.

[53] D.J. Bacon, A.F. Calder, F. Gao, V.G. Kapinos, S.J. Wooding, Nucl. Instrum. Meth. B 102 (1995) 37.

[54] C.A. English, M.L. Jenkins, Mater. Sci. Forum 15–18 (1987) 1008.

[55] L.R. Greenwood, J. Nucl. Mater. 216 (1994) 29.

[56] R.E. Stoller, J. Nucl. Mater. 237 (1997) 999.

[57] T. Diaz de la Rubia, M.W. Guinan, Phys. Rev. Lett. 66 (1992) 2766.

[58] T. Diaz de la Rubia, W. Phythian, J. Nucl. Mater. 191–194 (1992) 108.

[59] T. Diaz de la Rubia, Annul Rev. Mater. Sci. 26 (1996) 613.

[60] J. Lindhard, M. Scharff, H.E. Schøtt, K. Dan. Vidensk. Selsk. Mat. Fys. Medd. 33 (1963) 14.

[61] T. Diaz de la Rubia, G.H. Gilmer, Phys. Rev. Lett. 74 (1995) 2507.

[62] J.Q. Broughton, X.-P. Li, Phys. Rev. B 35 (1987) 9120.

[63] W.D. Luedtke, U. Landman, Phys. Rev. B 37 (1988) 4656.

[64] I. Kwon et al., Phys. Rev. B 41 (1990) 3678.

[65] M.H. Grabow, G.H. Gilmer, A.F. Baker, in: J. Tersoff et al. (Eds.), Atomic Scale Calculations in Materials Science, MRS Symposia Proceedings No. 141, Materials Research Society, Pittsburgh, PA, 1989, p. 349.

[66] L.A. Marques, M.J. Caturla, T. Diaz de la Rubia, J. Appl. Phys. 80 (1996) 6160.

[67] J.B. Gibson et al., Phys. Rev. 120 (1960) 1229.

[68] M.D. Giles, J. Electrochem. Soc. 138 (1991) 1160.

[69] P. Sigmund, Appl. Phys. Lett. 14 (1969) 114.

[70] R.J. Schreutelkamp, J.S. Custer, J.R. Liefting, W.X. Lu, F.W. Saris, Mater. Sci. Rep. 6 (1991) 1.

[71] H.L. Heinisch, Nucl. Instrum. Meth. B 102 (1995) 47.

[72] H. Wollenberger, in: R.W. Cahn, P. Haasen (Eds.), North-Holland, Amsterdam, 1983, p. 1140.

[73] H.E. Scheafer, D. Butteweg, W. Dander, Defects in High Purity Iron after 27 K Electron Irradiation, in: M.T. Robinson, F.W. Young, Jr. (Eds.), Proc. Int. Conf on Fundamental

Aspects of Radiation Damage in Metals, Gatlinburg, 1975, CONF-751006, Mater. Techn. Inf. Service, Springfield, VZ, 22161, p. 463.

[74] H. Trinkhaus, B.N. Singh, A.J.E. Foreman, J. Nucl. Mater. 199 (1992) 5.

[75] H. Trinkhaus, B.N. Singh, A.J.E. Foreman, J. Nucl. Mater. 206 (1993) 200.

[76] L. Pelaz, G.H. Gilmer, Appl. Phys. Lett., in press.

[77] J. Zhu, T. Diaz de la Rubia, C. Maihot, Phys. Rev. B 54 (1996) 4741.

[78] R J. Borg, G.J. Dienes, Introduction to Solid State Diffusion, Academic Press, San Diego, 1988.

[79] S. Tian, S.J. Morris, B. Obradovic, M.F. Morris, G. Wang, G. Balamurugan, A.F. Tasch, C. Snell, UT-Marlowe, Version 4.0.

[80] M.-J. Caturla, T. Diaz de la Rubia, Mater. Res. Soc. Boston (1996) in press.

[81] E. Collart, Mater. Res. Soc. Symp. (1997) in press.

[82] A. Agarway, Mater. Res. Soc. Symp. (1997).